On the Application of the Dynamic Smagorinsky Model to Large-Eddy Simulations of the Cloud-Topped Atmospheric Boundary Layer

M. P. KIRKPATRICK*
Center for Turbulence Research, Stanford University, Stanford, California

A. S. ACKERMAN
NASA Ames Research Center, Moffett Field, California

D. E. STEVENS
Lawrence Livermore National Laboratory, Livermore, California

N. N. MANSOUR
Center for Turbulence Research, Stanford University, Stanford, California

(Manuscript received 16 February 2005, in final form 17 June 2005)

ABSTRACT

In this paper the dynamic Smagorinsky model originally developed for engineering flows is adapted for simulations of the cloud-topped atmospheric boundary layer in which an anelastic form of the governing equations is used. The adapted model accounts for local buoyancy sources, vertical density stratification, and poor resolution close to the surface and calculates additional model coefficients for the subgrid-scale fluxes of potential temperature and total water mixing ratio. Results obtained with the dynamic model are compared with those obtained using two nondynamic models for simulations of a nocturnal marine stratocumulus cloud deck observed during the first research flight of the second Dynamics and Chemistry of Marine Stratocumulus (DYCOMS-II) field experiment. The dynamic Smagorinsky model is found to give better agreement with the observations for all parameters and statistics. The dynamic model also gives improved spatial convergence and resolution independence over the nondynamic models. The good results obtained with the dynamic model appear to be due primarily to the fact that it calculates minimal subgrid-scale fluxes at the inversion. Based on other results in the literature, it is suggested that entrainment in the DYCOMS-II case is due predominantly to isolated mixing events associated with overturning internal waves. While the behavior of the dynamic model is consistent with this entrainment mechanism, a similar tendency to switch off subgrid-scale fluxes at an interface is also observed in a case in which gradient transport by small-scale eddies has been found to be important. This indicates that there may be problems associated with the application of the dynamic model close to flow interfaces. One issue here involves the plane-averaging procedure used to stabilize the model, which is not justified when the averaging plane intersects a deforming interface. More fundamental, however, is that the behavior may be due to insufficient resolution in this region of the flow. The implications of this are discussed with reference to both dynamic and nondynamic subgrid-scale models, and a new approach to turbulence modeling for large-eddy simulations is proposed.

1. Introduction

The popularity of the large-eddy simulation (LES) technique in atmospheric research is due in part to the difficulties involved with obtaining sufficient field data to develop and test theories concerning the structure and dynamics of the boundary layer. LESs provide three-dimensional time-evolving velocity and scalar fields at a resolution limited only by the computational resources. As such, LES is often used to isolate particular physical processes of interest, such as boundary layer entrainment (Stevens et al. 2000) or transition from one cloud type to another (Wyant et al. 1997). It is also used to generate databases of different atmospheric flow regimes in order to evaluate, refine, and develop parameterization schemes for use in large-scale

* Current affiliation: School of Engineering, University of Tasmania, Tasmania, Australia.

Corresponding author address: Michael Kirkpatrick, School of Engineering, Private Bag 65, University of Tasmania, Hobart, Tasmania 7001, Australia.
E-mail: michael.kirkpatrick@utas.edu.au

models (cf. Lappen and Randall 2001). At the other end of the spectrum, LES is used as a platform on which to develop accurate models of cloud microphysics and radiation (Ackerman et al. 2004).

Despite an increasing reliance on LES as a tool for developing and testing boundary layer theories, there is still uncertainty concerning the fidelity of the simulations themselves. While LES has been shown to be relatively robust for simple cases such as simulations of a clear, convective boundary layer (Mason 1989), model intercomparisons for more complex cases have shown large variations in predictions of important statistics and bulk parameters. In the 1995 Global Energy and Water Cycle Experiment (GEWEX) Cloud System Studies (GCSS) Working Group 1 model intercomparison, for example, Bretherton et al. (1999) compared simulations of a smoke cloud beneath a temperature inversion. In this case, radiative cooling at the top of the cloud drives convection, which leads to entrainment and growth of the boundary layer. The authors found that the entrainment rates and other statistics predicted by the various LES codes differed by up to a factor of 2. The recent intercomparison of simulations of trade cumuli by Stevens et al. (2001) is a second example. Here again, important parameters such as stratiform cloud fraction and the variance of total water mixing ratio were found to be sensitive to the choice of numerical method, spatial resolution, and subgrid-scale turbulence model. Bulk parameters such as boundary layer height, entrainment rate, liquid water path, and cloud fraction are important variables in the parameterizations used in global circulation models. It is therefore essential that LES be made robust in its prediction of these variables if it is to be used as a tool for development and tuning of parameterizations for large-scale models.

The results of these model intercomparisons indicate that the difficulties encountered are related predominantly to the presence of a strong temperature inversion at cloud top, and positive and negative feedback loops involving turbulent entrainment across the inversion, radiation, and cloud microphysics. These feedback loops tend to make simulation results very sensitive to details of the numerics and subgrid-scale model. Consequently, over the past few decades considerable effort has been devoted to developing subgrid-scale (SGS) turbulence models that are better able to parameterize the physical processes occurring within the cloud layer. Much of this work has involved taking parameterizations developed for neutral boundary layers and deriving corrections to account for buoyancy effects associated with the background stratification and local buoyancy sources due to latent heat exchange within the cloud (cf. Lilly 1962; Deardorff 1980; Mason 1989; MacVean and Mason 1990). In this paper we contribute to this effort by presenting an adaption of the dynamic Smagorinsky model of Germano et al. (1991) for atmospheric simulations.

In contrast to other SGS models in which the model coefficients must be prescribed a priori, dynamic SGS models compute the model coefficients dynamically during the simulation itself, using information contained in the resolved flow fields. For this reason, dynamic models can be considered self-calibrating, a feature that makes them an appealing choice for dealing with the complex interactions between the hydrodynamics, radiation, and cloud microphysics occurring within clouds. While dynamic SGS models have been used with considerable success for complex engineering flows (cf. Boivin et al. 2000; Branley and Jones 2001), their application to atmospheric flows has been very limited. Sullivan and Moeng (1992) tested the dynamic Smagorinsky model for buoyancy-driven flows and discussed its application to atmospheric LES. Their formulation for the addition of a buoyancy correction to the standard dynamic Smagorinsky model uses an iterative solution procedure that was found to be computationally expensive and to suffer from stability problems, requiring the application of additional constraints to ensure stable convergence. While Sullivan and Moeng obtained good results for Rayleigh–Bérnard flow at a low Reynold's number, tests of their dynamic model in the atmospheric LES model of Moeng (1984) gave results that diverged considerably from similarity theory close to the surface. They concluded that the dynamic model does not function correctly in this region because most of the energy is contained in the subgrid scales.

More recently, Porté-Agel et al. (2000) applied a dynamic SGS model to simulations of the clear, neutral atmospheric boundary layer (ABL). To overcome deficiencies in the standard model close to the surface, they generalized the dynamic procedure by removing the assumption that the model coefficient is independent of length scale. They found that their "scale-dependent dynamic model" gives improved results in the near-surface region. Cederwall (2002) used the standard dynamic Smagorinsky model in simulations of the stable, clear ABL. To give appropriate fluxes through the near-surface layer Cederwall added a variation of a near-surface model developed by Brown et al. (2001). Cederwall also calculated the turbulent Prandtl number dynamically, but did not include an explicit stability correction in the model. Workers T. S.

Lund et al. (2004, personal communication) performed a similar study of a weakly stable boundary layer using the dynamic Smagorinsky model, but used the mean eddy viscosity prescription of Sullivan et al. (1994) in the near-surface region. They claim that effects of stability are accounted for automatically in the model, so that there is no need to use "ad hoc stability corrections" or to calculate the turbulent Prandtl number dynamically. Esau (2004) performed simulations of Ekman boundary layers using the dynamic mixed model of Zang et al. (1993), and found that this model gives improved performance over the dynamic Smagorinsky model in the near-surface region. Chow et al. (2005) applied a dynamic model based on an explicit filtering approach to simulation of a neutral boundary layer. In the near-surface region, they used a near-surface model similar to that used by Cederwall.

The investigations described above all focused on simulations of the dry ABL and used the Boussinesq form of the governing equations, which enabled them to adopt the standard form of the dynamic models developed for incompressible engineering flows. Of these studies, only Sullivan and Moeng (1992) attempted simulations of an unstable boundary layer or attempted to use a formulation that includes an explicit buoyancy correction, and those authors do not claim to have obtained satisfactory results.

In this paper we adapt the dynamic Smagorinsky model for simulations of the cloud-topped ABL using an anelastic form of the governing equations. Rather than relying on the dynamic procedure to account for stability effects, our model includes explicitly the buoyancy correction of Lilly (1962). A similar correction was used by Sullivan and Moeng (1992); however, we formulate this term in a way that circumvents the need for iteration and overcomes the stability issues associated with their formulation. We note here that, contrary to the assertion of T. S. Lund et al. (2004, personal communication), our tests showed that the inclusion of this correction gives significant differences in the results. We also argue that this stability correction is far from "ad hoc," as it is derived from a balance between turbulence production and dissipation in the turbulence kinetic energy (TKE) equation. In our model, eddy diffusivities for each of the scalar variables such as potential temperature and total water mixing ratio are also calculated dynamically. As with the stability correction, preliminary tests showed that calculating these diffusivities dynamically gave significant differences when compared with simulations in which a constant turbulent Prandtl number was used. The main focus of this study is on the performance of the dynamic model in the cloud layer and in particular, close to the temperature inversion. For this reason, we follow Cederwall (2002) and Chow et al. (2005) and adopt the relatively simple near-surface layer model of Brown et al. (2001) to give the correct transfer of fluxes between the surface and the well-resolved region of the simulation.

Our adapted dynamic model is compared with two commonly used nondynamic models in simulations of a nocturnal marine stratocumulus cloud deck observed during the first research flight of the second Dynamics and Chemistry of Marine Stratocumulus (DYCOMS-II) field experiment (Stevens et al. 2003a). One of the primary aims of this experiment was to characterize the conditions to such an extent that LESs of the case could be closely constrained. In 2003, data collected during the first research flight (RF01) of DYCOMS-II formed the basis for another GCSS model intercomparison, the results of which are described by Stevens et al. (2005). The case was found to be particularly challenging, with a large variation in the results obtained with different LES models.

The results presented in this paper were obtained using an atmospheric LES code developed for boundary layer clouds, the Distributed Hydrodynamic Aerosol and Radiation Model Application (DHARMA; Stevens and Bretherton 1996; Stevens et al. 2000, 2002). The adapted dynamic SGS model is implemented in the new LES Length Scale and Model Coefficient Algorithms (LLAMA) code presented here. LLAMA is a FORTRAN90 module that provides a suite of SGS models. It is designed to "plug into" existing hydrodynamics solvers, which may be serial or parallel using Message Passing Interface (MPI). In addition to the adaptation of the dynamic Smagorinsky model presented here, LLAMA also includes an adapted version of the dynamic mixed model of Zang et al. (1993) and localized versions of the dynamic Smagorinsky and dynamic mixed models, using the localized dynamic procedure of Piomelli and Liu (1995). A complete description of the SGS models provided by LLAMA is given in Kirkpatrick et al. (2003).

2. Overview of test case and simulations

The case chosen for the simulations is based on results obtained during the first research flight of the DYCOMS-II field experiment. Measurements were taken in and above a nocturnal stratocumulus-topped boundary layer situated over the Pacific Ocean off the west coast of California. Little or no drizzle was recorded below the cloud deck during the flight, and precipitation was limited to droplet sedimentation within the cloud.

The computational domain extends 3.2 km in the two

horizontal directions and 1.5 km in the vertical direction. Simulations are run on a grid with 96 × 96 × 128 cells in the x, y, and z directions, respectively. Cell spacing is uniform in the horizontal directions with cells of width $\Delta x = \Delta y = 33$ m and is stretched in the vertical direction to give cells of height $\Delta z = 4.35$ m close to the bottom surface and in the vicinity of the temperature inversion capping the ABL. These are the same grid and domain size as those used for the DHARMA simulations presented in the intercomparison referred to above. To assess the effect of spatial resolution, we also run simulations on a lower-resolution (64 × 64 × 96) and a higher-resolution (128 × 128 × 172) grid. The grid parameters are summarized in Table 1.

The boundary conditions imposed are periodic boundaries in the horizontal directions, a zero flux condition at the top boundary, and fixed surface fluxes for all variables at the bottom boundary. Sedimentation of liquid water is neglected here. The domain coordinates move with the geostrophic winds to reduce numerical errors. The spatial discretization is based on the third-order Modified Utopia (MU) scheme, while time integration uses a second-order Runge–Kutta scheme (Stevens and Bretherton 1996). The equations are integrated over a period of 4 h with analysis performed for the final 2 h of the simulations. Further details of the parameters defining the case, including initial conditions and external forcings, along with the results of the associated GCSS model intercomparison, are described by Stevens et al. (2005).

TABLE 1. Grids used for the simulations: Δx, Δy, and Δz are the cell dimensions in the x, y, and z directions, respectively. Here $\Delta = (\Delta x \Delta y \Delta z)^{1/3}$ is the filter width (see section 4).

Grid	Δx (=Δy)	$\Delta z_{\min}$	$\Delta_{\min}$
64 × 64 × 96	50.0	6.25	25.0
96 × 96 × 128	33.3	4.35	16.7
128 × 128 × 172	25.0	3.25	12.5

3. Governing equations

The dynamics of the cloud-topped atmospheric boundary layer can be described using equations for conservation of mass, momentum, liquid water potential temperature, and total water mixing ratio. These equations are written in the anelastic form of Ogura and Phillips (1962) in which the thermodynamic variables are decomposed into an isentropic base state, corresponding to a uniform potential temperature, and a dynamic component. Following Clark (1979), the dynamic component is further decomposed into an initial environmental deviation in hydrostatic balance and a time-evolving dynamic perturbation. For example, the decomposition for pressure is given by

$$p(x, y, z, t) = p_0(z) + p_1(z) + p_2(x, y, z, t), \qquad (1)$$

where subscript 0 refers to the isentropic base state, subscript 1 refers to the initial deviation, and subscript 2 refers to the dynamic perturbation. Similar decompositions are used for potential temperature and density. After subtracting hydrostatic balances, the resulting continuous equations are written as

$$\frac{\partial \varrho_0 u_i}{\partial t} + \frac{\partial (\varrho_0 u_i u_j)}{\partial x_j} = -\frac{\partial p_2}{\partial x_i} + \delta_{i3} g \frac{\varrho_0 \theta_{v2}}{\theta_0} - \epsilon_{ijk} \varrho_0 f_j u_k + H_{u_i}, \qquad (2)$$

$$\frac{\partial \varrho_0 \theta_l^*}{\partial t} + \frac{\partial (\varrho_0 \theta_l^* u_j)}{\partial x_j} = H_{\theta_l^*}, \qquad (3)$$

$$\frac{\partial \varrho_0 q_t}{\partial t} + \frac{\partial (\varrho_0 q_t u_j)}{\partial x_j} = H_{qt}, \quad \text{and} \qquad (4)$$

$$\frac{\partial (\varrho_0 u_j)}{\partial x_j} = 0. \qquad (5)$$

Here u_i are the Cartesian components of the velocity vector, ϱ is the density, δ_{ij} is the Kronecker delta, ϵ_{ijk} is the permutation tensor, f_j is the Coriolis parameter, g is the acceleration due to gravity, q_t is the total water mixing ratio, and $\theta_l^* = (\theta_l - \theta_0)/\theta_0$ is a scaled liquid water potential temperature. Total water mixing ratio is the sum of the liquid and vapor mixing ratios,

$$q_t = q_c + q_v = \frac{\varrho_c + \varrho_v}{\varrho_d}, \qquad (6)$$

where ϱ_c, ϱ_v, and ϱ_d are the mass density of the condensed water, water vapor, and dry air, respectively. Liquid water potential temperature is defined as

$$\theta_l = \theta - \frac{L}{C_{pd} \pi_{\text{hyd}}} q_c. \qquad (7)$$

Here L is the latent heat of vaporization, C_{pd} is the specific heat at constant pressure for dry air, and

$$\pi_{\text{hyd}} = \left(\frac{p_0 + p_1}{p_{\text{ref}}} \right)^{R_d/C_p},$$

with p_{ref} being a reference pressure of 1000 mbar and R_d being the gas constant of dry air. The virtual potential temperature θ_v appearing in the buoyancy term of the momentum equations is given by

$$\theta_v = \theta \left[1 + \left(\frac{R_d}{R_v} - 1 \right) q_v - q_c \right], \qquad (8)$$

where R_v is the gas constant for water vapor. The terms H_{u_i}, $H_{\theta_l^*}$, and H_{q_t} are source terms that include parameterizations for physical processes such as radiation and subsidence.

In an LES, the equations are filtered to remove from the solution the turbulent fluctuations that cannot be resolved by the numerical method. For the anelastic equations it is convenient to use a density-weighted or Favre filter, where a Favre-filtered variable is defined as $\tilde{\phi} = \overline{\varrho\phi}/\overline{\varrho}$. Application of this filter to the equations gives

$$\frac{\partial \overline{\varrho}_0 \tilde{u}_i}{\partial t} + \frac{\partial (\overline{\varrho}_0 \tilde{u}_i \tilde{u}_j)}{\partial x_j} = -\frac{\partial \overline{p}_2}{\partial x_i} + \delta_{i3} g \frac{\overline{\varrho}_0 \tilde{\theta}_{v2}}{\theta_0} - \epsilon_{ijk} \overline{\varrho}_0 \tilde{u}_k f_j + H_{u_i} - \frac{\partial \tau_{ij}}{\partial x_j}, \tag{9}$$

$$\frac{\partial \overline{\varrho}_0 \tilde{\theta}_l^*}{\partial t} + \frac{\partial (\overline{\varrho}_0 \tilde{\theta}_l^* \tilde{u}_j)}{\partial x_j} = H_{\theta_l^*} - \frac{\partial \gamma_{\theta_l^*}}{\partial x_j}, \tag{10}$$

$$\frac{\partial \overline{\varrho}_0 \tilde{q}_t}{\partial t} + \frac{\partial (\overline{\varrho}_0 \tilde{q}_t \tilde{u}_j)}{\partial x_j} = H_{qt} - \frac{\partial \gamma_{q_t}}{\partial x_j}, \quad \text{and} \tag{11}$$

$$\frac{\partial (\overline{\varrho}_0 \tilde{u}_j)}{\partial x_j} = 0, \tag{12}$$

with subgrid-scale stresses and fluxes given by

$$\tau_{ij} = \overline{\varrho}_0 (\widetilde{u_i u_j} - \tilde{u}_i \tilde{u}_j), \tag{13}$$

$$\gamma_{\theta_l^*} = \overline{\varrho}_0 (\widetilde{\theta_l^* u_j} - \tilde{\theta}_l^* \tilde{u}_j), \quad \text{and} \tag{14}$$

$$\gamma_{q_t} = \overline{\varrho}_0 (\widetilde{q_t u_j} - \tilde{q}_t \tilde{u}_j). \tag{15}$$

We have assumed here that f_j is constant so that the Coriolis term is linear. The source terms H are shown without an overbar since they are parameterizations rather than exact terms.

4. Subgrid-scale models

The most commonly used models for atmospheric LESs are based on the model first proposed in the early 1960s by Smagorinsky (1963) and Lilly (1962). The subgrid-scale stress is written as

$$\tau_{ij}^a = \tau_{ij} - \frac{1}{3} \delta_{ij} \tau_{kk} = -2 \overline{\varrho}_0 K_m \tilde{D}_{ij}, \tag{16}$$

where $\tilde{D}_{ij}$ is the strain rate tensor:

$$\tilde{D}_{ij} = \frac{1}{2} \left(\frac{\partial \tilde{u}_i}{\partial x_j} + \frac{\partial \tilde{u}_j}{\partial x_i} \right) - \frac{1}{3} \delta_{ij} \frac{\partial \tilde{u}_k}{\partial x_k}. \tag{17}$$

Here and elsewhere in this paper the superscript a is used to denote the anisotropic part of a tensor. The eddy viscosity K_m is given by

$$K_m = C \Delta^2 |\tilde{D}| C_B, \tag{18}$$

where $|\tilde{D}| = (2\tilde{D}_{ij}\tilde{D}_{ij})^{1/2}$, Δ is the filter width, approximated here as $\Delta = (\Delta x \Delta y \Delta z)^{1/3}$, and C is a dimensionless coefficient. In the nondynamic versions of the model this coefficient is a constant parameter and is often written as the Smagorinsky coefficient $c_s = C^{1/2}$. Following Mason (1985), the buoyancy correction term C_B is given by

$$\begin{aligned} C_B &= (1 - \mathrm{Ri}/\mathrm{Pr}_t)^{1/2} \quad && \mathrm{Ri}/\mathrm{Pr}_t < 1 \\ C_B &= 0 && \mathrm{Ri}/\mathrm{Pr}_t \geq 1, \end{aligned} \tag{19}$$

where the gradient Richardson number Ri is defined as

$$\mathrm{Ri} = \frac{N^2}{|\tilde{D}|^2}, \tag{20}$$

with the buoyancy frequency N given by

$$N^2 = \frac{g}{\theta_0} \frac{\partial \tilde{\theta}_v}{\partial z}. \tag{21}$$

In 1980, Deardorff (1980) proposed an additional stability correction in which the subgrid-scale mixing length is related to the TKE. While Deardorff originally used this correction with a prognostic TKE equation model, we use it here to modify the length scale in the Smagorinsky model. The new mixing length is written as

$$\begin{aligned} L &= \Delta [c_1 (1/\mathrm{Ri} - 1) - c_{e1}]/c_2 \quad && N^2 > 0, \\ L &= \Delta && N^2 \leq 0, \end{aligned} \tag{22}$$

where

$$\begin{aligned} c_1 &= c_a (0.76^2), \\ c_2 &= c_{e2} + 2c_1, \\ c_a &= 0.10, \\ c_{e1} &= 0.19, \quad \text{and} \\ c_{e2} &= 0.51. \end{aligned} \tag{23}$$

The eddy viscosity is then calculated as

$$\begin{aligned} K_m &= c_3 c_\epsilon^{-1/2} L^2 |\tilde{D}| C_B \quad && L > 0, \\ K_m &= 0 && L \leq 0, \end{aligned} \tag{24}$$

where

$$\begin{aligned} c_\epsilon &= c_{e1} + c_{e2} L/\Delta \quad \text{and} \\ c_3 &= c_a^{3/2}. \end{aligned} \tag{25}$$

In neutral and unstable conditions, this model gives an eddy viscosity equal to that calculated by the standard Smagorinsky formulation when the Smagorinsky coefficient is set to $c_s = 0.19$.

In addition to the buoyancy corrections outlined above, the Smagorinsky model requires further modification to account for poor spatial resolution of the flow field close to the surface. For the present work a damping function (Mason 1994) is applied to the model length scale in this region. Modeling the turbulence in the near-surface region is discussed further in section 5.

The distinguishing feature of a dynamic SGS model is that the model coefficient is not set to a single, fixed value at the start of the simulation. Instead, the coefficient is calculated dynamically during the simulation and can vary in time and space. To achieve this, a test filter is applied to the velocity and scalar variable fields to extract information from the smallest resolved scales. Application of a spatial test filter, denoted here by a caret (^), to the filtered momentum equations gives

$$\frac{\partial \widehat{\overline{\varrho}_0 \tilde{u}_i}}{\partial t} + \frac{\partial (\widehat{\overline{\varrho}_0 \tilde{u}_i \tilde{u}_j})}{\partial x_j} = -\frac{\partial \hat{\overline{p}}_2}{\partial x_i} + \delta_{i3} g \frac{\widehat{\overline{\varrho}_0 \tilde{\theta}_{v2}}}{\theta_0} - \epsilon_{ijk} \widehat{\overline{\varrho}_0 \tilde{u}_k} f_j + H_{ui} - \frac{\partial \hat{\tau}_{ij}}{\partial x_j}. \tag{26}$$

To rewrite this equation in a form similar to Eq. (9) we adopt a Favre test filter $\breve{\phi} = \widehat{\varrho \phi}/\hat{\varrho}$ giving

$$\frac{\partial \hat{\overline{\varrho}}_0 \breve{\tilde{u}}_i}{\partial t} + \frac{\partial (\hat{\overline{\varrho}}_0 \breve{\tilde{u}}_i \tilde{u}_j)}{\partial x_j} = -\frac{\partial \hat{\overline{p}}_2}{\partial x_i} + \delta_{i3} g \frac{\hat{\overline{\varrho}}_0 \breve{\tilde{\theta}}_{v2}}{\theta_0} - \epsilon_{ijk} \hat{\overline{\varrho}}_0 \breve{\tilde{u}}_k f_j + H_{u_i} - \frac{\partial \hat{\tau}_{ij}}{\partial x_j}. \tag{27}$$

In our case this equation can be simplified considerably by using a two-dimensional horizontal test filter rather than a three-dimensional one. The simplification stems from the fact that the density in our governing equations varies only in the z direction. A horizontal Favre test filter is then equivalent to a spatial test filter:

$$\breve{\phi} \equiv \hat{\phi}, \tag{28}$$

and the density field is left unchanged by the test-filtering operation:

$$\hat{\overline{\varrho}}_0 = \overline{\varrho}_0. \tag{29}$$

Another advantage of using a horizontal test filter is that it avoids commutation errors that would occur if the discrete filter were applied in the vertical direction where the grid is nonuniform (Ghosal and Moin 1995). Implicit in this is the assumption that the grid filter is also two-dimensional (Carati et al. 2001). This is a reasonable assumption in most ABL simulations, where the horizontal grid dimensions are typically larger than the vertical dimension.

Applying Eqs. (28) and (29) to Eq. (27) and using the fact that

$$\varrho_2 = \frac{\varrho_0 \theta_{v2}}{\theta_0} \tag{30}$$

gives

$$\frac{\partial \overline{\varrho}_0 \hat{\tilde{u}}_i}{\partial t} + \frac{\partial (\widehat{\overline{\varrho}_0 \tilde{u}_i \tilde{u}_j})}{\partial x_j} = -\frac{\partial \hat{\overline{p}}_2}{\partial x_i} + \delta_{i3} \hat{\overline{\varrho}}_2 g - \epsilon_{ijk} \overline{\varrho}_0 \hat{\tilde{u}}_k f_j + H_{u_i} - \frac{\partial \hat{\tau}_{ij}}{\partial x_j}. \tag{31}$$

Extracting the resolved stress $\mathcal{L}_{ij} = \overline{\varrho}_0 (\widehat{\tilde{u}_i \tilde{u}_j} - \hat{\tilde{u}}_i \hat{\tilde{u}}_j)$ then gives

$$\frac{\partial \overline{\varrho}_0 \hat{\tilde{u}}_i}{\partial t} + \frac{\partial (\overline{\varrho}_0 \hat{\tilde{u}}_i \hat{\tilde{u}}_j)}{\partial x_j} = -\frac{\partial \widehat{\overline{p}_2}}{\partial x_i} + \delta_{i3} \hat{\overline{\varrho}}_2 g - \epsilon_{ijk} \overline{\varrho}_0 \hat{\tilde{u}}_k f_j + H_{u_i} - \frac{\partial \hat{\tau}_{ij}}{\partial x_j} - \frac{\partial \mathcal{L}_{ij}}{\partial x_j}. \tag{32}$$

Alternatively, application of the grid and test filters together to the continuous equations gives

$$\frac{\partial \overline{\varrho}_0 \hat{\tilde{u}}_i}{\partial t} + \frac{\partial (\overline{\varrho}_0 \hat{\tilde{u}}_i \hat{\tilde{u}}_j)}{\partial x_j} = -\frac{\partial \widehat{\overline{p}_2}}{\partial x_i} + \delta_{i3} \hat{\overline{\varrho}}_2 g - \epsilon_{ijk} \overline{\varrho}_0 \hat{\tilde{u}}_k f_j + H_{u_i} - \frac{\partial T_{ij}}{\partial x_j}, \tag{33}$$

where T_{ij} is the SGS stress at the test filter level:

$$T_{ij} = \overline{\varrho}_0 (\widehat{\tilde{u}_i \tilde{u}_j} - \hat{\tilde{u}}_i \hat{\tilde{u}}_j). \tag{34}$$

Comparison of Eqs. (32) and (33) gives the Germano identity:

$$\mathcal{L}_{ij} = T_{ij} - \hat{\tau}_{ij}. \tag{35}$$

The basic assumption underlying the dynamic procedure is that the model used to parameterize the SGS stress at the grid filter level τ_{ij} can also be used to parameterize the SGS stress at the test filter level T_{ij}, and that the model coefficient remains the same in both cases. Using this, the test level stress is written as

$$T_{ij}^a = -2 \overline{\varrho}_0 C \hat{\Delta}^2 |\hat{\tilde{D}}| \hat{\tilde{D}}_{ij} \hat{C}_B, \tag{36}$$

where $\hat{C}_B$ is given by

$$\begin{aligned} \hat{C}_B &= (1 - \widehat{\mathrm{Ri}}/\widehat{\mathrm{Pr}}_t)^{1/2} \quad \widehat{\mathrm{Ri}}/\widehat{\mathrm{Pr}}_t < 1 \\ \hat{C}_B &= 0 \qquad\qquad\qquad\quad \widehat{\mathrm{Ri}}/\widehat{\mathrm{Pr}}_t \geq 1, \end{aligned} \tag{37}$$

with the test level Richardson number given by

$$\widehat{\mathrm{Ri}} = \frac{\widehat{N^2}}{|\hat{\tilde{D}}|^2} = \frac{g/\theta_0 \partial \hat{\tilde{\theta}}_v/\partial z}{|\hat{\tilde{D}}|^2}. \tag{38}$$

In our formulation, the Prandtl number is calculated as $\mathrm{Pr}_t = C/C_\theta$, where C and C_θ are the model coefficients calculated for momentum and liquid water potential temperature during the previous time step. It is reasonable to use the values from the previous time step because these coefficients are averaged over horizontal planes (see below) and vary slowly in time. We note also that, in our formulation, $\widehat{Pr}_t \equiv \mathrm{Pr}_t$ since Pr_t varies only in the vertical direction and the test filter acts only in the horizontal directions. This procedure requires no iteration and was found to be stable for a variety of test cases.

Substituting the parameterizations for the subgrid-scale stress τ_{ij} [Eq. (16)] and test level stress T_{ij} [Eq. (36)] into the Germano identity [Eq. (35)] gives

$$\begin{aligned} \overline{\varrho}_0(\widehat{\tilde{u}_i\tilde{u}_j} - \hat{\tilde{u}}_i\hat{\tilde{u}}_j)^a = &-2\overline{\varrho}_0 C\hat{\Delta}^2|\hat{\tilde{D}}|\hat{\tilde{D}}_{ij}\hat{C}_B \\ &+ 2\widehat{\overline{\varrho}_0 C\Delta^2|\tilde{D}|\tilde{D}_{ij}}C_B. \end{aligned} \tag{39}$$

Removing the constant factor $\overline{\varrho}_0$, contracting tensors using the least squares approach of Lilly (1992), and assuming C is constant on horizontal planes then gives an equation for the model coefficient,

$$C\Delta^2 = -\frac{\langle M_{ij}\mathcal{L}_{ij}^{*a}\rangle}{\langle 2M_{kl}M_{kl}\rangle}, \tag{40}$$

where

$$\mathcal{L}_{ij}^{*} = \widehat{\tilde{u}_i\tilde{u}_j} - \hat{\tilde{u}}_i\hat{\tilde{u}}_j \quad \text{and} \tag{41}$$

$$M_{ij} = \alpha^2|\hat{\tilde{D}}|\hat{\tilde{D}}_{ij}\hat{C}_B - \widehat{|\tilde{D}|\tilde{D}_{ij}}C_B. \tag{42}$$

Here, α is the ratio of the test and grid filter widths

$$\alpha = \hat{\Delta}/\Delta. \tag{43}$$

The angle brackets indicate averaging on horizontal planes, which is necessary to stabilize the dynamic procedure (Germano et al. 1991). The consequences of using this averaging procedure in ABL simulations are discussed in section 8.

The Smagorinsky model for the subgrid-scale flux of potential temperature θ_l^* is written as

$$\gamma_{\theta_l^*} = -\overline{\varrho}_0 C_\theta \Delta^2 |\tilde{D}| \frac{\partial \tilde{\theta}_l^*}{\partial x_j} C_B. \tag{44}$$

Applying the dynamic procedure outlined above to the equation for conservation of potential temperature [Eq. (3)] gives an analogous equation for the model coefficient:

$$C_\theta \Delta^2 = -\frac{\langle F_j E_j\rangle}{\langle F_k F_k\rangle}, \tag{45}$$

where the resolved flux E_j is given by

$$E_j = \widehat{\tilde{\theta}_l^*\tilde{u}_j} - \hat{\tilde{\theta}}_l^*\hat{\tilde{u}}_j, \tag{46}$$

and

$$F_j = \alpha^2|\hat{\tilde{D}}|\frac{\partial \hat{\tilde{\theta}}_l^*}{\partial x_j}\hat{C}_B - \widehat{|\tilde{D}|\frac{\partial \tilde{\theta}_l^*}{\partial x_j}}C_B. \tag{47}$$

The model for the SGS flux of q_t is identical, with θ_l^* replaced by q_t.

In the following sections we present and discuss results obtained using the models described above. We will refer to the models using the following abbreviations: SM—Smagorinsky model with Lilly stability correction, SMD—Smagorinsky model with Lilly stability correction and additional stability correction of Deardorff, and DSM—dynamic Smagorinsky model (also includes Lilly stability correction).

5. Modeling near-surface turbulence

Modeling turbulence in the region close to the surface presents a challenge for both dynamic and nondynamic SGS models. At high Reynolds numbers, according to Prandtl's mixing length hypothesis, the size of the energetic eddies is proportional to the distance from a solid boundary. It is inevitable that below some height, these energetic eddies will no longer be resolved by the grid. This is a fundamental problem for the LES technique itself, since the theoretical foundations of the approach are based on the assumption that the large, energetic eddies are resolved and only the small dissipative scales need to be modeled. Because the small scales of turbulence tend to be isotropic and dissipative, a relatively simple turbulence model is generally considered to be adequate to parameterize their effects on the resolved motions. This is in contrast to Reynolds stress or "RANS" models, which are formulated for use with the Reynolds-averaged Navier–Stokes equations. These models tend to be considerably more complex than LES models because they attempt to parameterize all the scales of turbulence. LES subgrid-scale models, such as the Smagorinsky model, cannot be expected to

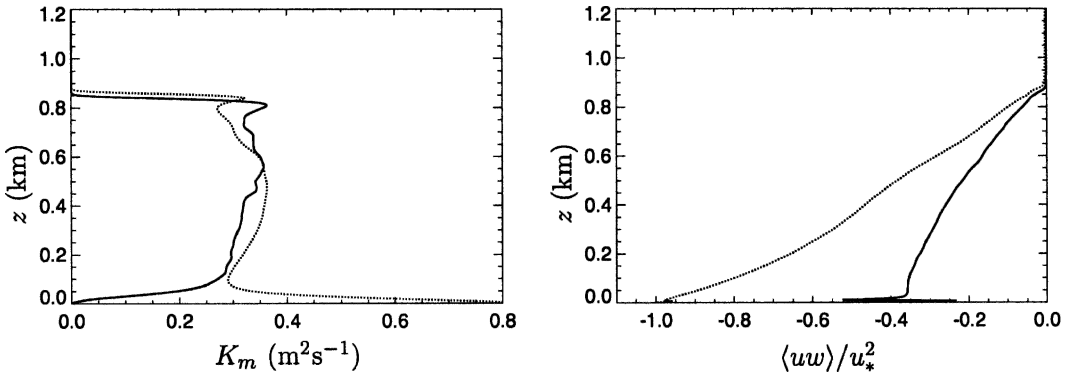

FIG. 1. Profiles of (left) eddy viscosity and (right) total shear stress for standard DSM (solid line) and SMD (dotted line).

accurately parameterize turbulence when the energetic scales of turbulence are not well resolved.

A number of researchers have proposed approaches aimed at addressing this problem. In 1975, Schumann (1975) developed a model that behaved like an LES model in the outer layer and a RANS model close to the wall. In 1992 Mason and Thomson (1992) proposed a stochastic backscatter model, which attempts to include the effects of the spectral backscatter of energy from small to large scales that has been found to occur in poorly resolved regions of flow. Sullivan et al. (1994) suggested a hybrid LES–RANS model similar to that of Schumann. Their model aims to include the effects of anisotropy observed in turbulent flow fields close to solid surfaces. In the same year, Mason (1994) suggested using a damping function to reduce the model length scale near the surface. Kosović (1997) proposed a nonlinear model that aims to address both the issues of anisotropy and backscatter.

For the nondynamic Smagorinsky models, SM and SMD, we use the approach of Mason (1994) mentioned above. The model length scale is modified in the region close to the surface using a damping function,

$$\frac{1}{\Delta^{*2}} = \frac{1}{\Delta^2} + \left(\frac{c_s}{kz}\right)^2, \tag{48}$$

where k is the von Kàrmàn constant. With the dynamic model, a modification such as this is not appropriate, since the quantity calculated by the dynamic procedure is $C\Delta^2$, which includes the length scale Δ [see Eq. (40)]. Some form of modification is necessary, however, as the dynamic model in its standard form tends to give insufficient SGS diffusion in the near-surface region.

Evidence of this is seen in Fig. 1, which shows vertical profiles of the eddy viscosity K_m and the total shear stress $\langle uw \rangle$ obtained with the dynamic Smagorinsky model (DSM) and the nondynamic Smagorinsky model with Deardorff correction (SMD). The total shear stress is the sum of the resolved and subgrid-scale shear stresses in the predominant wind direction and is normalized by the mean surface shear stress u_*^2. All results in this section are for simulations performed on the $96 \times 96 \times 128$ cell grid with statistics averaged over horizontal planes and over the time period $t = 2$–4 h.

Above 100 m, the profiles of eddy viscosity calculated by DSM and SMD are similar. Below this height, however, the two models diverge markedly. As the surface is approached, the eddy viscosity calculated by DSM approaches zero while that calculated by SMD increases to a value more than 2 times that seen in the remainder of the boundary layer. An increase in eddy viscosity is expected in this region, as more of the turbulence energy is contained in the subgrid scales. Thus it appears that close to the surface DSM is outside its range of applicability. As with the SGS models themselves, the dynamic procedure is based on the assumption that the energetic scales of turbulence are well resolved. Since this assumption is not valid in the near-surface layer, the dynamic procedure does not accurately calculate the model coefficient in this region. This is in accordance with the findings of other investigators (cf. Porté-Agel et al. 2000; Cederwall 2002; Chow et al. 2005).

A consequence of the poor representation of the near-surface turbulence by DSM is seen in the shear stress profile in Fig. 1. The boundary layer in this simulation is well mixed, so the primary force balance is between the turbulent stresses and the large-scale, horizontal pressure gradient. We therefore expect the shear stress to follow an approximately linear profile going from u_*^2 at the surface to zero at the inversion. (A small deviation from the linear profile is expected because of the effects of the Coriolis acceleration.) The SMD simulation gives a good approximation to this expected

profile. The DSM simulation, on the other hand, drastically underpredicts the stress throughout the boundary layer, and gives a large "wiggle" close to the surface. These errors are due to the fact that the model is not transferring sufficient momentum across the near-surface layer.

One possible approach to resolving this problem is to use a modified form of the dynamic procedure to calculate the Smagorinsky model coefficient. An example of this is the scale-dependent dynamic model of Porté-Agel et al. (2000). Results obtained with this model indicate that it calculates the Smagorinsky coefficient more accurately in poorly resolved regions such as the near-surface layer. An alternative and simpler approach adopted by Cederwall (2002) is to combine the standard dynamic model with a separate "near-surface model" that is specifically designed to parameterize the subgrid-scale fluxes close to the surface. This approach is appealing because it uses the dynamic Smagorinsky model only where the assumptions implicit in its derivation are valid, namely, away from the surface. We have adopted a similar approach here.

The near-surface model used by Cederwall is based on a model originally proposed by Brown et al. (2001) for LES of a laboratory-scale rough wall boundary layer. Brown et al. used the Smagorinsky model with stochastic backscatter of Mason and Thomson (1992) as the base SGS model. To provide additional SGS momentum transfer across the near-surface region, they added a "canopy stress" of the form

$$\tau_c = -\int C_c a(z) \varrho_0 |\mathbf{u}| u_i \, dz. \tag{49}$$

Here, $|\mathbf{u}|$ is the horizontal wind speed and $C_c a(z)$ represents a canopy density function, which has units of area divided by volume. Brown et al. used a canopy density function in which $a(z) = \cos^2(\pi z/2h_c)$ for $z \leq h_c$, where h_c is the height of the canopy, and $a(z) = 0$ for $z > h_c$. The canopy height was based on the geometry of the wire mesh used as a roughening device on the surface of the wind tunnel. They set C_c empirically so that the mean velocity at the top of the canopy matched the experimental data. The constant of integration is set such that $\tau_c = 0$ at the top of the near-surface region. Using this model, Brown et al. obtained numerical results that are in close agreement with the expected logarithmic-law velocity profile near the surface.

Cederwall (2002) adapted the canopy stress model for use in combination with the dynamic Smagorinsky model. In place of the $\cos^2$ profile, Cederwall used a $\cos^3$ profile. This was found to be sufficient to ensure a smooth transition between the well-resolved region and the near-surface layer. Also, rather than tuning the model coefficient C_c to give the expected velocity profile, this coefficient is calculated dynamically, such that the total stress at the first grid point above the wall is equal to the local wall shear stress u_*^2. This is consistent with the fact that, when the dynamic Smagorinsky model is used, both resolved and SGS shear stresses approach zero at the surface. Last, Cederwall sets the canopy height equal to the horizontal grid spacing $h_c = \Delta x$, which is assumed to be representative of the scale of the smallest resolved eddies. Cederwall tested this combination of near-surface and dynamic model in simulations of the neutral ABL and found that it gives a very good prediction of the log-law velocity profile in the surface layer.

Recently Chow et al. (2005) followed the work of Cederwall but combined the near-surface model with a more complex dynamic SGS model developed using an explicit filtering approach. They also ran simulations of the neutral ABL and again found that this combination of near-surface and dynamic models gives excellent prediction of the log-law velocity profile in the surface layer.

In this paper we also follow the formulation of Cederwall with one modification. We set the canopy height to be $h_c = 2(\Delta x \Delta y \Delta z_1)^{1/3}$, where Δz_1 is the height of the cells in the bottom layer of the grid. The length scale $2(\Delta x \Delta y \Delta z)^{1/3}$ is frequently used in LES as an approximation for the size of the smallest resolved eddies (Scotti et al. 1997) and has the advantage that it takes into account the spatial resolution in all directions. It is also the same as the length scale 2Δ used to represent the filter width in our application of the Smagorinsky model. (In the Smagorinsky model, the factor of 2 is absorbed into the model coefficient.) In the analogous models for potential temperature and water, $|\mathbf{u}|$ in Eq. (49) is replaced by θ_l^* and q_t, respectively.

Figure 2 shows a comparison of shear stress profiles obtained with DSM and SMD, similar to that shown in Fig. 1. This time, however, the DSM simulation uses the near-surface model. The large wiggle seen in Fig. 1 is almost gone, and the DSM simulation now gives a good approximation to the expected linear stress profile, indicating that the combined model is giving a realistic representation of the fluxes through the near-surface layer. (We believe that the small wiggle seen in the results for both SMD and DSM is artificial and is due to the fact that the analysis does not include fluxes introduced by the numerical method.)

Figure 3 shows the total shear stress $\langle uw \rangle$ and the three components that combine to produce it—namely, the resolved shear stress $\langle \tilde{u}\tilde{w} \rangle$, SGS shear stress τ_{13}, and the canopy stress τ_c generated by the near-surface

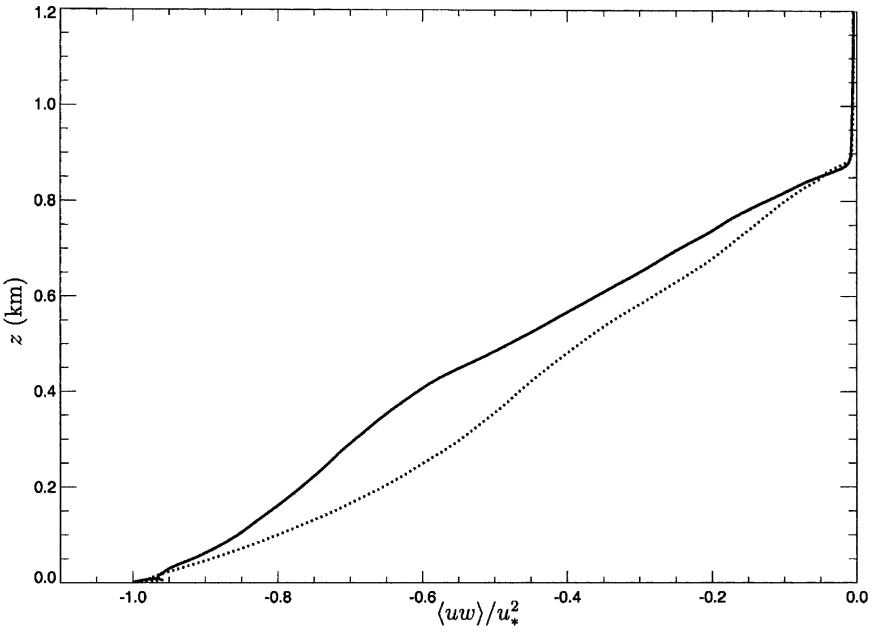

FIG. 2. Profiles of total shear stress normalized by u_*^2: DSM (solid line) and SMD (dotted line).

model. Results are plotted on a semilogarithmic graph to highlight the behavior of the various components close to the surface. The resolved stress increases from zero at the top of the boundary layer to a peak at a height of approximately 30 m. It then decreases rapidly as the surface is approached. The height of 30 m corresponds closely to $2\Delta = 33.3$ m, thus supporting our argument that 2Δ is an appropriate scale for the canopy

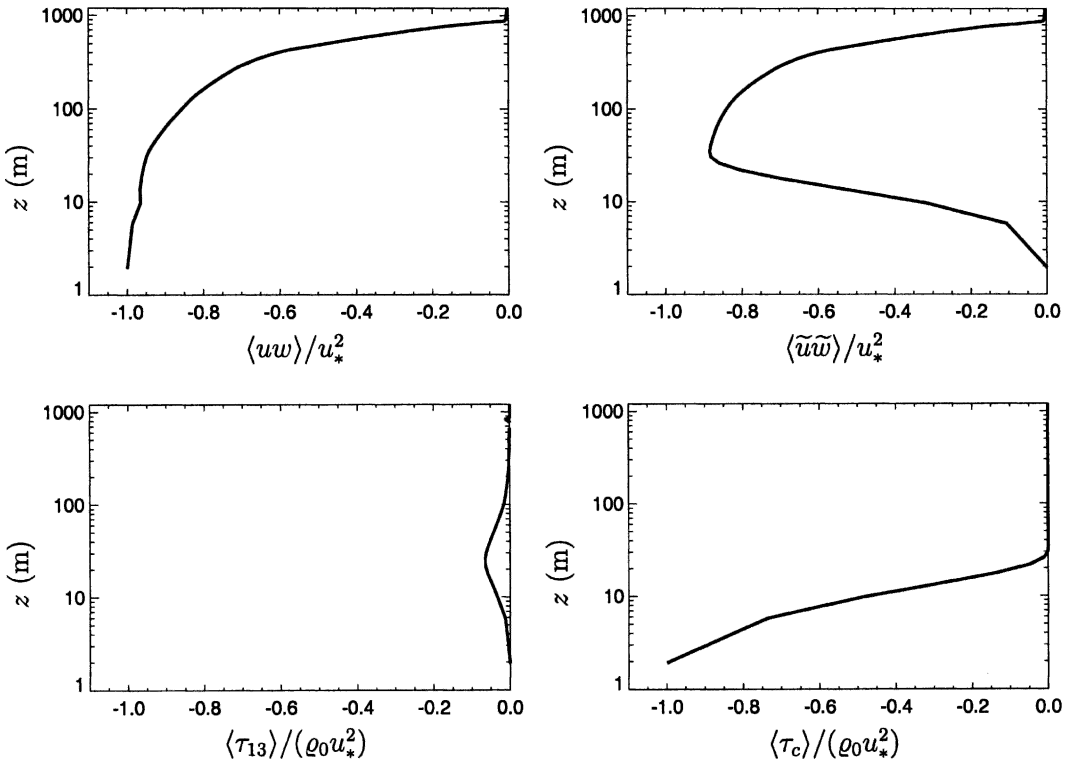

FIG. 3. Profiles of normalized total shear stress $\langle uw \rangle$, resolved shear stress $\langle \tilde{u}\tilde{w} \rangle$, SGS shear stress $\langle \tau_{13} \rangle$, and surface layer stress $\langle \tau_c \rangle$ for DSM with the near-surface model.

height. The canopy stress is seen to increase from zero at $h_c = 2\Delta = 33$ m to a value equal to the wall shear stress u_*^2 at the first node. The SGS stress bridges the remaining gap between the resolved stress and the canopy stress, reaching a peak at a height of approximately 25 m. The combined effect is to give a smooth transition between the boundary conditions applied at the surface and the well-resolved region of the flow.

6. Comparison with observational measurements

In this section we compare results obtained using the three SGS turbulence models described in section 4: the standard nondynamic SM, the nondynamic SMD, and our adapted version of the DSM, which also includes the Lilly stability correction. The nondynamic models use a constant model coefficient of $c_s = C^{1/2} = 0.18$ and a constant Prandtl number of $\mathrm{Pr}_t = 0.4$. The DSM simulation also uses the near-surface model described in the previous section.

The simulations are of the DYCOMS-II RF01 case described in section 2. During the first hour of simulation time, the numerical model "spins up" from the artificial initial conditions to a fully developed turbulent state. It is conceivable that the results during later times may be affected by the response of the SGS models to the artificial conditions during spinup. As we are interested only in how the SGS models function within a developed turbulent flow field, we run the first hour of all simulations with the SGS models turned off. The near-surface model is switched on during this spinup period to ensure that realistic fluxes are maintained through the near-surface region. The solution at $t = 1$ h then provides initial conditions for the simulations using the different SGS models, which are integrated over the remaining 3 h. The results presented in this section were calculated using the $96 \times 96 \times 128$ grid. Each simulation took approximately 4 h to run on 16 nodes of an Origin 3000 supercomputer at the National Aeronautics and Space Administration (NASA) Ames Research Center. The extra computational cost incurred when the dynamic model is used is typically 15%–20%.

Figure 4 shows time series of inversion height z_{inv}, cloud-base height z_{base}, liquid water path (LWP), and cloud fraction obtained with each model. (Here z_{inv} is defined as the height of the 8.0 g kg^{-1} isoline of q_r.) The entrainment rate E is calculated as

$$E = \frac{dz_{\mathrm{inv}}}{dt} - w_{\mathrm{sub}}. \tag{50}$$

Here, dz_{inv}/dt is calculated as the average rate of change of dz_{inv} over the period $t = 2$–4 h. The subsidence velocity w_{sub} is $-z_{\mathrm{inv}}$ (also averaged over $t = 2$–4 h) multiplied by the large-scale divergence, which for this case was prescribed to be 3.75×10^{-6} s^{-1} (see Stevens et al. 2005). Table 2 shows the entrainment rate calculated as described above, along with the z_{base}, cloud fraction, and LWP averaged over $t = 3$–4 h for the four models. The model results are compared with estimates obtained from the field measurements.

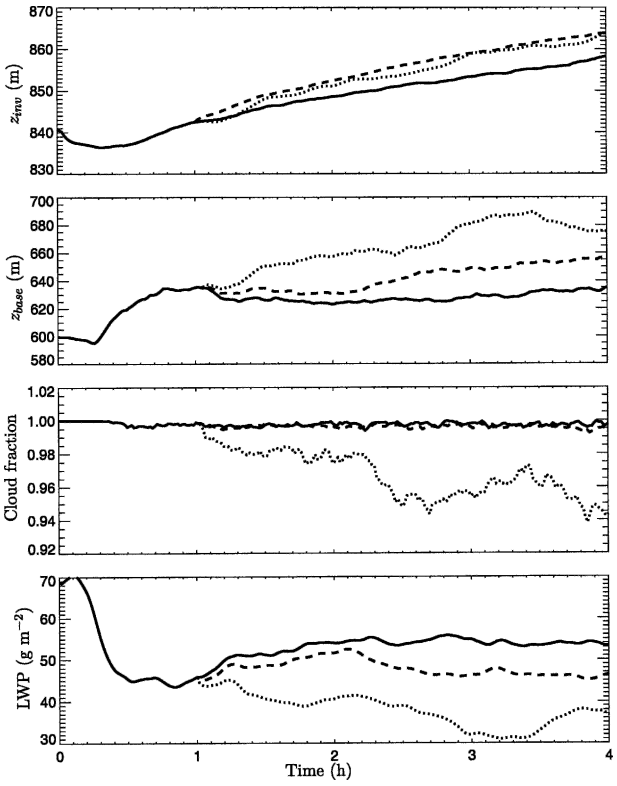

FIG. 4. Time series of (from top to bottom) inversion height, cloud-base height, cloud fraction, and LWP: DSM (solid line), SMD (dashed line), and SM (dotted line).

Overall the results for the DSM simulation are considerably closer to the observations for each parameter than are the results for the SM and SMD simulations. The entrainment rate of 0.44 cm s^{-1} calculated by DSM is relatively close to the measured value of 0.38 ± 0.1 cm s^{-1}, as compared with the entrainment rates of 0.48 and 0.51 cm s^{-1} calculated by SMD and SM, respec-

TABLE 2. Bulk parameters for the three models compared with the observations. Observational measurements are as shown in Stevens et al. (2003b).

	Measured value	DSM	SMD	SM
E (cm s^{-1})	0.38 ± 0.1	0.44	0.48	0.51
z_{base} (m)	600	630	650	680
Cloud fraction (%)	>99	99.7	99.6	95.7
LWP (g m^{-2})	62	54	46	34

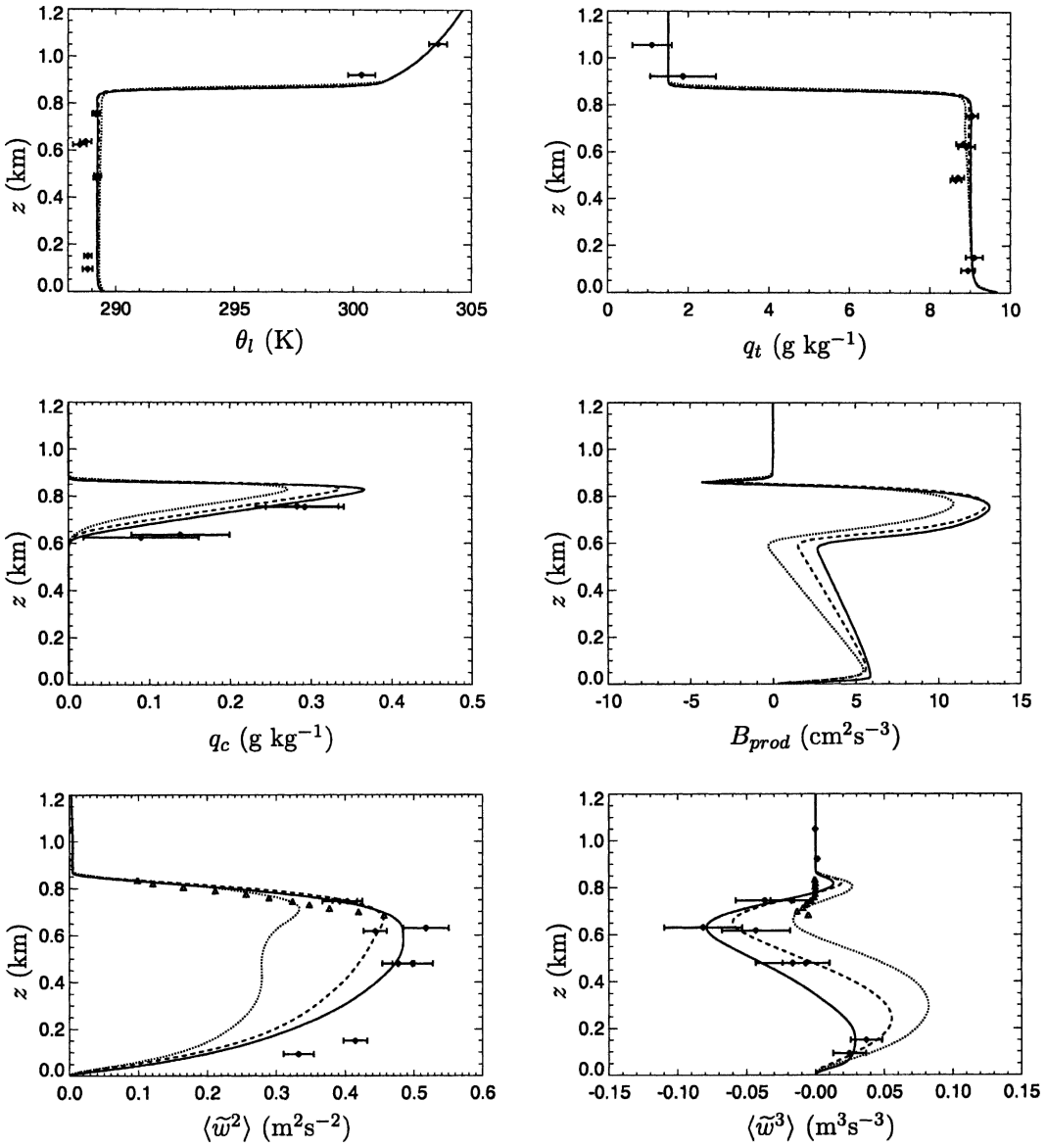

FIG. 5. Profiles of liquid water potential temperature, total water, condensed water, resolved buoyancy production, and the second and third moments of the resolved vertical velocity: DSM (solid line), SMD (dashed line), and SM (dotted line). Markers indicate in situ (diamond) and radar (triangle) measurements.

tively. These differences in entrainment rate are reflected in the results for the other three bulk parameters. DSM, with the lowest entrainment rate, calculates the lowest cloud-base height, the highest cloud fraction, and the highest LWP. At the other end of the scale, SM calculates the highest entrainment rate, and has the highest cloud-base height, lowest cloud fraction, and lowest LWP. The results for SMD lie between these two extremes.

Figure 5 shows profiles of the mean state variables and vertical velocity statistics for each model, overlayed with the observational data. All statistics presented here and below are averaged over the final 2 h, that is for t = 2–4 h. The profiles obtained with DSM and SMD for the mean state variables, θ_l, q_t, and q_c, are in good agreement with the observations. The SM simulation calculates a drier cloud, with q_c reduced by 20%–25% when compared with the other models. A similar trend is seen in the profile of resolved buoyancy production B_{prod}, which is also lower in the cloud layer for the SM simulation.

A larger variation in results is seen in the profiles of the vertical velocity statistics. For the second moment $\langle \tilde{w}^2 \rangle$, DSM again gives the best agreement with the ob-

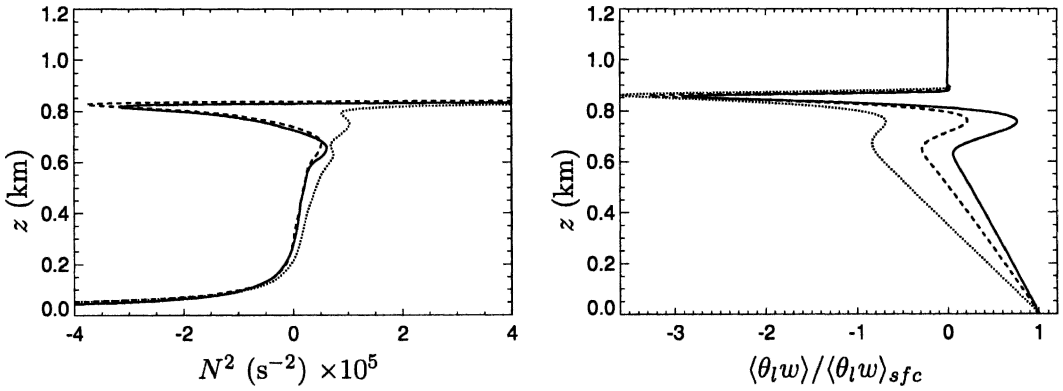

FIG. 6. Profiles of (left) buoyancy frequency and (right) the total vertical flux of liquid water potential temperature (normalized by the mean surface flux): DSM (solid line), SMD (dashed line), and SM (dotted line).

servations, lying within the error bars of the in situ measurements everywhere except at the lower two data points. [This discrepancy at the lower two data points was common to all the models in the GCSS intercomparison described by Stevens et al. (2005).] SMD gives a $\langle \tilde{w}^2 \rangle$ profile that is also in reasonable qualitative agreement with the observations but underpredicts the values slightly. The SM on the other hand, underpredicts $\langle \tilde{w}^2 \rangle$ by approximately 50% and calculates a two-peaked profile with a local minimum at cloud base, rather than the single-peaked profiles seen in the observations and the DSM and SMD results. A similar trend is seen in the third-moment profiles. The $\langle \tilde{w}^3 \rangle$ profiles for DSM and SMD are both in good agreement with the in situ measurements, while the profile calculated by SM lies well to the right of the observations. We discuss the reasons for these differences below.

A clear trend seen in these sounding results is the large difference between the results for SM and those for DSM and SMD. This is in contrast to the entrainment rate results, for which SM is relatively close to DSM and SMD. A similar trend is seen in the results for the bulk parameters listed in Table 2. This indicates that there is a critical entrainment rate somewhere between the entrainment rates calculated by SMD and SM. Above this critical point a negative feedback mechanism becomes active that tends to moderate any further increase in entrainment rate. We would expect such a critical point to be associated with a fundamental change in the nature of the flow field.

Evidence of this change is seen in Fig. 6, which shows profiles of the square of the buoyancy frequency N^2 and the total vertical flux of liquid water potential temperature $\langle \theta_l w \rangle$. These profiles show a significant difference in the stability profile calculated by the SM simulation relative to the profiles calculated by the other two models. While DSM and SMD calculate a cloud layer that is unstable (N^2 negative), the cloud layer calculated by SM is stable (N^2 positive).

The underlying cause of this difference in stability is seen in the profiles of the vertical flux of liquid water potential temperature. In the SM simulation, the direction of the θ_l flux is downward throughout the cloud layer, whereas, in the DSM and SMD simulations, the direction of the flux is upward within the bulk of the cloud layer, and downward only at cloud top. The direction of the θ_l flux depends on the balance between the downward flux of warm air entrained across the inversion and the upward flux due to radiative cooling at cloud top. In the DSM and SMD simulations, this balance remains in favor of radiative cooling, producing an unstable cloud layer, whereas in the SM simulation, drying of the cloud reduces cloud-top radiative cooling tipping the balance in favor of a net downward flux and producing a stable cloud layer. By damping vertical motions, this statically stable layer acts as a local negative feedback mechanism that moderates further increases in the entrainment rate.

The difference in stability also explains the difference seen between the profiles of buoyancy production and the vertical velocity statistics. The reduction in B_{prod} in the SM simulation is due to a combination of the positive stability profile and drying of the cloud, which reduces the moisture available for evaporative cooling in downdrafts and also reduces the rate of radiative cooling at cloud top. Similarly, the single-peaked $\langle \tilde{w}^2 \rangle$ profiles seen in the results for DSM and SMD are typical of a well-mixed, slightly unstable boundary layer, whereas the attenuated, two-peaked $\langle \tilde{w}^2 \rangle$ profile seen in the SM results indicates a less energetic boundary layer and reduced mixing of the cloud and subcloud layers. These effects are due again to the positive stability profile and reduced buoyancy production that occur in the SM simulation. In addition to the local negative feedback

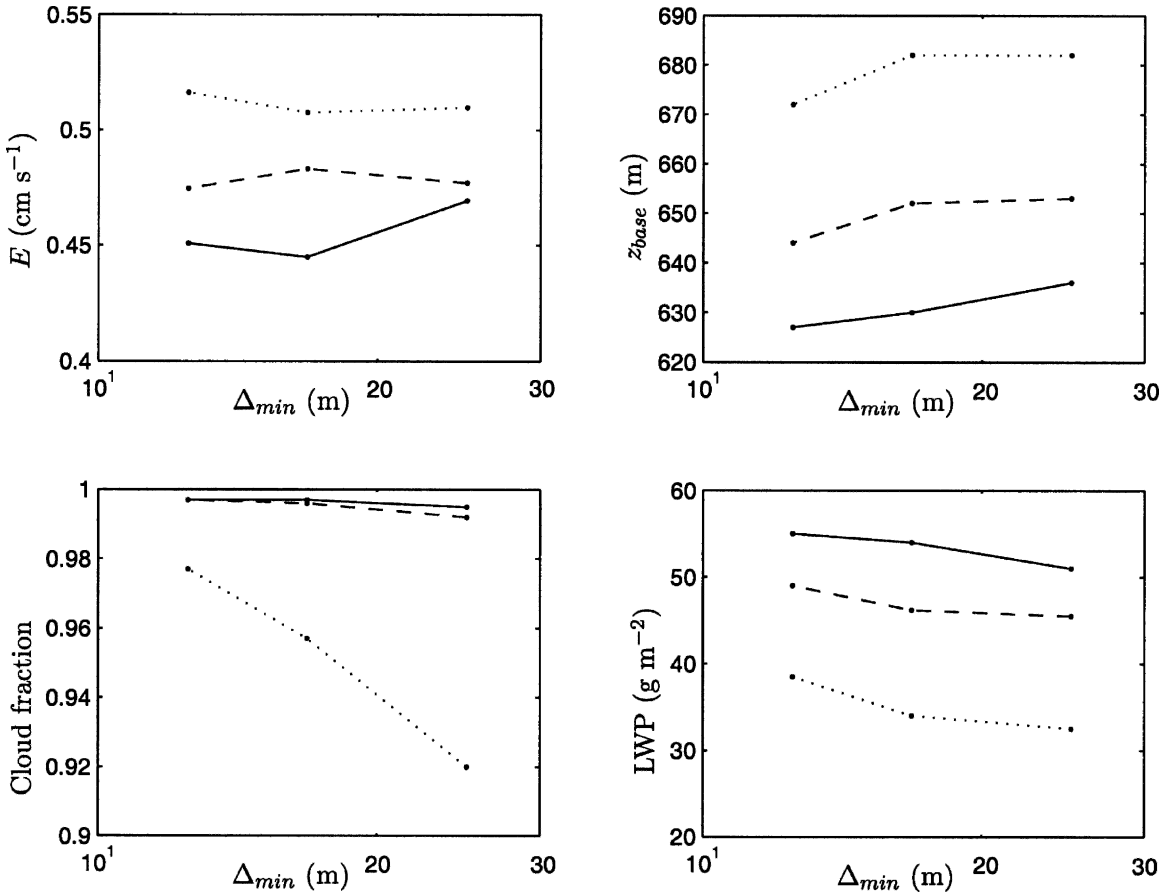

FIG. 7. Variation of bulk parameters with spatial resolution. Here Δ_{min} is the minimum filter size associated with each grid. (see Table 1). Statistics are calculated in the same manner as they were for Table 2: DSM (solid line), SMD (dashed line), and SM (dotted line).

mechanism described above, the less energetic boundary layer–scale motions in the SM simulation (as indicated by the attenuated $\langle \tilde{w}^2 \rangle$ profile) are also expected to moderate entrainment (Stevens et al. 2005). The reader is referred to the articles of Bretherton and Wyant (1997) and Stevens (2000) for further discussion of decoupling of stratocumulus-topped ABLs.

The S-shaped $\langle \tilde{w}^3 \rangle$ profiles produced by DSM and SMD result when cooling at cloud top leads to negatively buoyant downdrafts within the cloud layer that are of similar strength to the positively buoyant updrafts generated at the sea surface. In the SM simulation, the positive stability and reduced evaporative cooling weaken the downdrafts in the cloud layer, so that convective updrafts from the sea surface tend to dominate. Consequently the $\langle \tilde{w}^3 \rangle$ profile is moved to the right. The small region of positive $\langle \tilde{w}^3 \rangle$ seen at cloud top is not seen in the radar data; however, it is seen in the $\langle \tilde{w}^3 \rangle$ profiles of all the models in the GCSS intercomparison (Stevens et al. 2005). This discrepancy requires further investigation.

7. Effects of spatial resolution

In this section we consider the spatial convergence characteristics of each of the models. The role of an SGS model is to parameterize the effects of the unresolved scales of motion on the solution for the resolved scales. In this context, an ideal SGS model would ensure that the mean statistics and bulk parameters calculated by the LES model are independent of spatial resolution. To investigate the effects of spatial resolution, we repeated the simulations on a lower-resolution grid ($64 \times 64 \times 96$) and a higher-resolution grid ($128 \times 128 \times 172$) and compared them with the results obtained on the standard ($96 \times 96 \times 128$) grid. In each case the resolution at the surface is the same as the resolution at the inversion.

Figure 7 shows the variation with resolution of the bulk parameters: E, z_{base}, cloud fraction, and LWP, while Fig. 8 shows the variation in $\langle \tilde{w}^2 \rangle$ profiles. The results for DSM show trends typical of a smoothly converging model. The change in each parameter de-

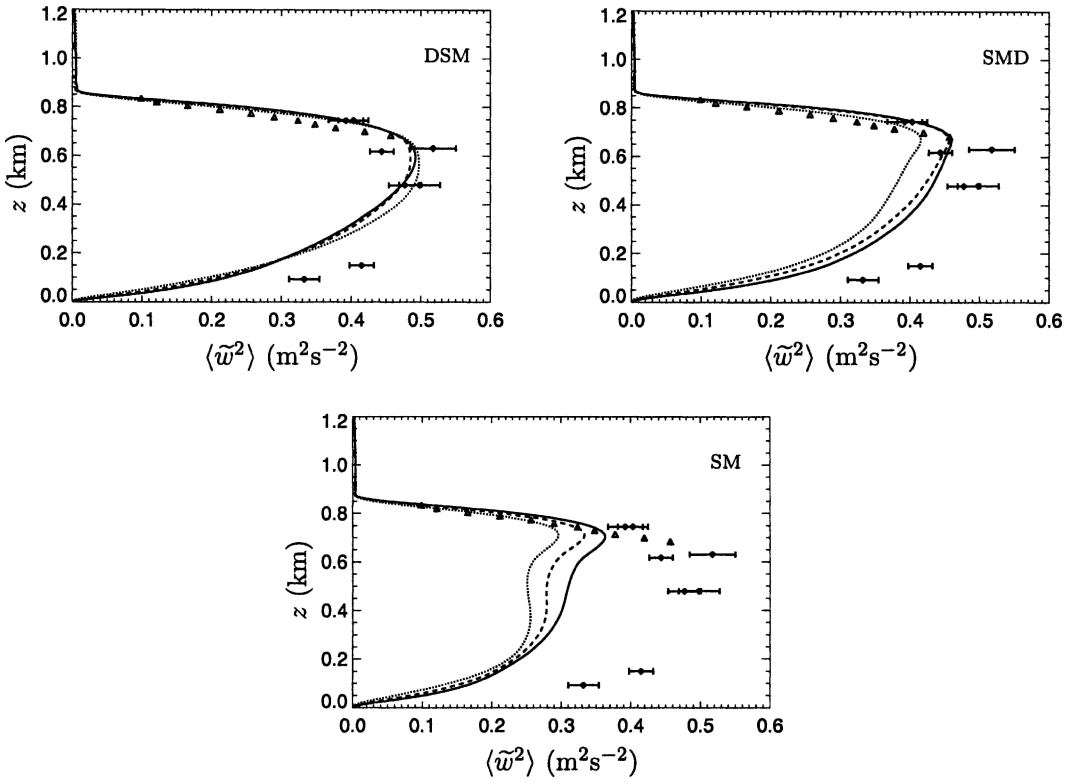

FIG. 8. Variation of the second moment of vertical velocity with spatial resolution for the three SGS models: 64 × 64 × 96 (dotted line), 96 × 96 × 128 (dashed line), and 128 × 128 × 172 (solid line).

creases as resolution is increased, with only a relatively small change in results as the resolution is increased from the standard to the high-resolution grid. These results indicate that a high degree of resolution independence has been achieved with DSM on the standard grid. The results for DSM are also converging toward values that are close to the observational results (see Table 2).

The SM and SMD results for cloud fraction, LWP, z_{base}, and $\langle \tilde{w}^2 \rangle$ are changing in the direction of the DSM and observational results. In the case of LWP and z_{base}, however, the change in results increases rather than decreases as resolution is increased. The trends for entrainment rate are not clear, especially for the SM simulations, which may be due to the fact that the SM simulation is close to the critical entrainment rate discussed above. Overall, the results indicate that the two nondynamic model simulations have not achieved the same degree of resolution independence on the standard grid as the DSM simulation. The results for SMD on the standard and high-resolution grids are relatively close to the DSM and observational results. In contrast, the results for SM remain far from the observations even on the high-resolution grid.

It is also important to verify the resolution independence of the dynamic procedure itself. As discussed in section 3, scale independence of the model coefficient is critical for DSM to function correctly, since the dynamic procedure assumes the same coefficient can be used at both the grid and test filter levels. Figure 9 shows the model coefficient calculated by DSM on the low-resolution, standard, and high-resolution grids. The near-surface layer shows some variation in the model coefficient, as we expect based on the discussion in section 5. Throughout the bulk of the boundary layer, however, the profiles demonstrate a high degree of resolution independence, especially for the standard and high-resolution simulations.

As well as demonstrating grid independence, comparisons of spatial convergence curves with experimental results are useful in detecting the presence of any significant oversights in the overall modeling of the system. As stated in the introduction, the DYCOMS-II field experiment was deliberately designed to provide sufficient data to closely constrain LESs. While our DSM results are generally close to the observations, Fig. 7 shows the entrainment rate converging toward an asymptotic value that is approximately 10% higher than the measured value, while LWP is converging toward a value approximately 10% lower than the observed

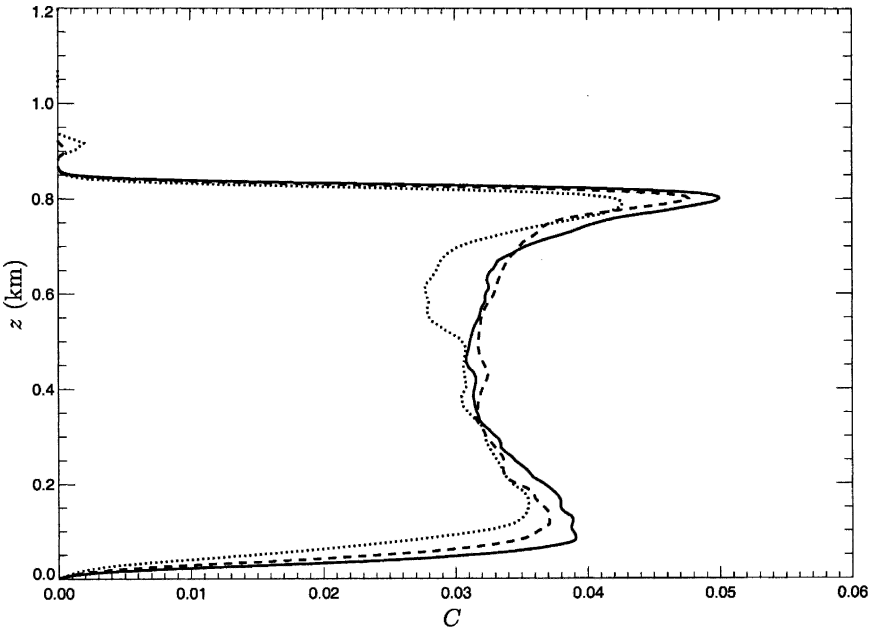

FIG. 9. Variation with spatial resolution of the model coefficient C calculated by DSM (note that $C = c_s^{1/2}$): $64 \times 64 \times 96$ (dotted line), $96 \times 96 \times 128$ (dashed line), and $128 \times 128 \times 172$ (straight line).

value. Assuming our numerical method is consistent (in the sense that solution to the discretized equations approaches the solution of the continuous equations as the size of the grid cells approaches zero), this discrepancy is indicative of some significant form of modeling error. A likely candidate is the absence of any model to account for the effects of droplet sedimentation within the cloud. For the present study we set conditions as prescribed for the GCSS intercomparison (Stevens et al. 2005) and so do not include the effects of droplet sedimentation. In a separate study, however, Ackerman et al. (2004) found that droplet sedimentation has a significant effect in simulations of the DYCOMS-II case, causing both an increase in LWP and a decrease in entrainment.

8. Discussion

The results presented above show the DSM simulation consistently giving significantly better agreement with the field data than the simulations using the nondynamic models, and also giving better resolution independence. What are the key differences in the behavior of the dynamic model that enable it to give these results?

Figure 10 shows a comparison of the eddy viscosity

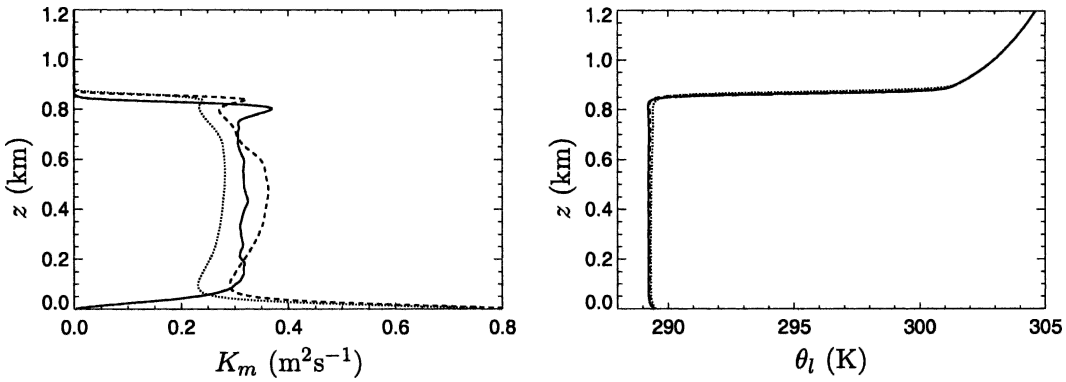

FIG. 10. (left) Profiles of eddy viscosity for DSM (solid line), SMD (dashed line), and SM (dotted line). The relative position of the inversion for each case is (right) indicated by the θ_l profile.

calculated by DSM, SMD, and SM. The relative position of the inversion for each case is indicated by the θ_l profile. Throughout most of the boundary layer, the eddy viscosity calculated by DSM is very similar to that calculated by SMD and SM. On reflection, this similarity is remarkable considering the different ways in which the model coefficient is calculated in each case. As described in section 4, SMD and SM use fixed model coefficients that are derived from physical arguments based on turbulence theory and from field measurements. DSM, on the other hand, calculates the model coefficients dynamically during the simulation itself from information contained in the resolved flow fields. This fact, when combined with the results in the previous sections, is strong evidence that DSM is functioning correctly throughout the bulk of the boundary layer.

There are two regions in which the eddy viscosity profiles calculated by the three models differ significantly: in the near-surface region and at cloud top. In the near-surface region the eddy viscosity calculated by DSM approaches zero as the surface is approached, leading to unrealistically low fluxes across the near-surface layer. In section 5 we argued that DSM could not be expected to perform well in this region because the turbulence is poorly resolved and so the model is outside its range of applicability. Consequently, we supplemented the dynamic SGS model with a near-surface model in order to ensure that realistic fluxes are maintained across this layer.

At cloud top, the profiles show two obvious differences between the eddy viscosity calculated by DSM and that calculated by the nondynamic models. The first is that DSM calculates a higher eddy viscosity at cloud top. The second is that the eddy viscosity profile calculated by DSM approaches zero just below the inversion, whereas the profiles calculated by SM and SMD approach zero just within the inversion. Both of these factors are expected to contribute to the lower entrainment rate calculated by DSM. A higher eddy viscosity at cloud top damps in particular the smaller-scale resolved motions in this region, hence reducing the kinetic energy available in these eddies for entrainment. A lower eddy viscosity and eddy diffusivity within the inversion, on the other hand, reduce entrainment directly, by decreasing the SGS transport across the inversion. As we have seen, an accurate calculation of the entrainment rate appears to be a critical factor in achieving close agreement with the observations for the other statistics. Consequently, these differences in the behavior of the SGS models at cloud top play an important role in determining the overall results of each simulation.

Considering the two mechanisms outlined above in the context of the SM and SMD results presented here, we note that SM gives a lower eddy viscosity than SMD both within the inversion and at cloud top and yet gives a higher entrainment rate. This would seem to indicate that it is in fact the first mechanism that is more important in this case. That is, the lower eddy viscosity calculated by SM at cloud top leads to higher resolved TKE in this region, which results in more rapid entrainment. This argument may be oversimplistic, however, since it is based on comparisons of profiles generated by averaging over time and space, whereas the buoyancy corrections that actually cause the differences act locally. A further complication here results from the negative feedback loops discussed in section 6 whereby increased entrainment in the SM simulation leads to a cloud layer that is statically stable. This statically stable layer damps resolved vertical motions, while also causing a reduction in the eddy viscosity via the buoyancy correction term in the SM model.

We focus now on the second mechanism, whereby the eddy viscosity calculated by DSM drops to zero just below the inversion. A clear trend seen in the GCSS model intercomparison for the DYCOMS-II case (Stevens et al. 2005) was that the models that gave the best agreement with the observations used an SGS parameterization that, either through design or through a posteriori modification, gave zero SGS flux within the inversion. The DHARMA simulations using DSM were consistently closer to the observations than all except one of the other models. In that model the subgrid fluxes of scalar variables were manually switched off to test the importance of this effect. These findings raise an intriguing question about the physical processes associated with entrainment for this case. How can we simultaneously argue that all the flux across the inversion is being carried by the resolved scales, while at the same time argue that the eddy size is so small that it warrants turning off the SGS model?

One possible answer to this is that small eddy transport does in fact contribute significantly to the entrainment process for this case; however, in the simulations this transport is already adequately "parameterized" by the extra numerical diffusion associated with the monotone advection scheme used for the scalar variables. Thus, an SGS model that switches off in the entrainment layer is actually compensating fortuitously for excessive numerical diffusion.

A more interesting possibility, at least from a physical perspective, is that the dominant entrainment mechanism transport for this case is in fact one in which the resolved motions are primarily responsible for entrainment and that gradient transport by small eddies,

which forms the basis for eddy viscosity–based SGS parameterizations, is negligible. Support for this hypothesis is provided by the work of Fernando and Hunt (1997) and McGrath et al. (1997) who performed theoretical and experimental studies of entrainment mechanisms at shear-free density interfaces. They found that when the bulk Richardson number Ri_b is greater than 15, the dominant entrainment mechanism involves the generation of internal waves within the inversion by eddies impinging on the interface. Under certain circumstances the internal waves overturn and "break." The resulting local static instability then generates turbulent mixing that is responsible for entrainment. For bulk Richardson numbers significantly higher than 15, they found that entrainment is due almost exclusively to this breaking wave mechanism. The bulk Richardson number is defined as $\mathrm{Ri}_b = \Delta b L_h / u_h^2$, where Δb is the buoyancy jump, L_h is the integral length scale of the turbulence, and u_h is the integral velocity scale.

We argue that the situation at cloud top in the DYCOMS-II case is very similar to the situation analyzed by Fernando and Hunt (1997) and McGrath et al. (1997). Turbulence production is predominantly due to buoyancy production within the cloud rather than shear. The case is also in the stable regime with regard to thermodynamically driven instabilities associated with the cloud-top entrainment instability (using the criteria defined by MacVean and Mason 1990). One of the characteristics of the DYCOMS-II case is the strength of the inversion, with a potential temperature jump of approximately 12 K, giving a buoyancy jump of approximately 0.3 $\mathrm{m\,s^{-2}}$. The integral length scale for eddies within the cloud layer is of the order of 100 m, while, from inspection of the LES velocity fields, the integral velocity scale is of the order of 1 $\mathrm{m\,s^{-1}}$. This gives a bulk Richardson number on the order of 30. We therefore expect the wave-breaking mechanism described above to be the dominant mode of entrainment for this case. This mechanism is characterized by propagating internal waves and isolated breaking events, both of which can only be represented in the resolved component of the simulations. Gradient diffusion in nonoverturning regions of the interface does not contribute significantly to entrainment.

We conclude that, for the DYCOMS-II case, an SGS model that "switches off" subgrid-scale fluxes at the inversion is probably acting in accordance with the physics of the entrainment process. While DSM gives this behavior, this does not prove that it is doing so for the right reason. A similar tendency to switch off SGS fluxes is also seen in the near-surface region where it has been found to have a detrimental effect on the simulation.

A more critical test case is required to address this issue. Such a case was investigated by Kirkpatrick and Armfield (2005), who compared experimental and LES results for a purging cavity flow in which the bulk Richardson number was much lower (of order unity). In this case saltwater is purged from a cavity by an overflow of freshwater. During the later stages of the purging process, when the density interface is low in the cavity, entrainment is also driven by large eddies impinging on the interface from above and deforming the interface. In this case, however, because of the lower buoyancy jump, dense fluid is ejected from the deforming interface in the form of wispy streamers. This so-called eddy-impingement mechanism was first suggested by Linden (1973) and was also identified by McGrath et al. (1997), who found that it is the dominant entrainment mechanism for cases with a bulk Richardson number of less than 15. Based on a comparison of experimental and LES results for the purging flow, Kirkpatrick and Armfield (2005) suggested that, in addition to the large energetic eddies that deform the interface, smaller eddies close to the interface must also play an important role in the eddy-impingement entrainment mechanism and may be responsible for the generation of the streamers. When a large eddy deforms the interface, there are typically regions where the interface is close to vertical. In these regions the motion of small eddies across the interface is no longer inhibited by buoyancy forces, so these eddies are able to contribute to the entrainment process. Since the small eddies responsible for this mode of interfacial transport typically fall below the grid resolution they need to be parameterized by the SGS model. In the simulation, however, DSM showed similar behavior to that seen in the DYCOMS-II case, calculating minimal SGS fluxes at the interface. This led to a significant underprediction of the entrainment rate for the purging cavity flow.

From inspection of the LES results for the purging flow, Kirkpatrick and Armfield (2005) found that the dynamic procedure tends to predict negative values for the model coefficient on the nonturbulent side of the interface and positive values on the turbulent side. When the model coefficient is averaged over a horizontal plane that cuts through the deforming interface, the plane will typically include regions that are both above and below the interface, so that negative and positive values for the model coefficient tend to cancel out. The result of this is that the model coefficient approaches zero close to the interface. The authors noted that the plane-averaging procedure used to stabilize the dynamic procedure is usually justified based on an assumption of homogeneous turbulence. This assumption

is not valid on a plane that intersects a deforming interface, since the plane will contain zones of both nonturbulent flow and turbulent flow. This issue could be addressed relatively easily by using a localized dynamic model, such as the model of Piomelli and Liu (1995). An adapted version of this model is included in the LLAMA module (see Kirkpatrick et al. 2003) but has yet to be thoroughly tested.

It also seems likely, however, that the behavior of DSM at interfaces is a symptom of a more fundamental problem associated with insufficient resolution of the energetic eddies in these regions. This issue also has serious implications for nondynamic SGS models since, as stated previously, the basic assumption underlying the dynamic SGS model is essentially the same as that underlying all SGS models—namely, that the energetic scales of turbulence are well resolved. If the dynamic model is out of its range of applicability, then so too are all other SGS models.

9. Conclusions

In this paper, we have presented an adaptation of the dynamic Smagorinsky model for simulations of the cloud-topped atmospheric boundary layer. The adapted model accounts for buoyancy effects, vertical density stratification, and poor resolution close to the surface. It also calculates additional model coefficients for the subgrid-scale fluxes of liquid water potential temperature and total water mixing ratio. We have compared the adapted dynamic SGS model with two commonly used nondynamic SGS models for the DYCOMS-II RF01 case.

The dynamic model, DSM, performs significantly better than both of the nondynamic models, giving the closest agreement with the observations for all of the measured statistics. Of the nondynamic models tested in the present work, the Smagorinsky model with additional Deardorff stability correction, SMD, performs better than the standard Smagorinsky model, SM, which consistently gives relatively poor agreement with the observations. The critical feature of this case appears to be an accurate calculation of the entrainment rate. Excessive entrainment leads to drying of the cloud, which in turn reduces the rate of radiative cooling. In the SM simulation, this effect is strong enough to cause the development of a statically stable profile within the cloud layer, whereas both the DSM and SMD simulations maintain unstable conditions. We have suggested that a stable cloud layer provides a local negative feedback on entrainment by damping the vertical motions of eddies in the cloud-top region. Drying of the cloud in the SM simulation also leads to a less energetic boundary layer overall, which further moderates the entrainment rate by reducing the energy of the boundary layer–scale eddies. In the SMD simulation, the entrainment rate is also higher than the observed entrainment rate, however, the cloud layer remains statically unstable. Consequently, the SMD results for other statistics are considerably closer to the field data and to the results of the DSM simulation.

The difference in the entrainment rates calculated by the three models is related in particular to their behavior in the cloud-top region. Close to cloud top, DSM calculates the highest eddy viscosity, followed by SMD and then SM. Higher eddy viscosity causes greater damping of the resolved motions, reducing the kinetic energy available in the resolved eddies for the entrainment. A second difference between the dynamic and nondynamic models in this region is that the eddy viscosity profile calculated by DSM approaches zero just below the inversion, whereas the profiles calculated by SM and SMD approach zero just within the inversion. Therefore, SM and SMD are expected to give greater subgrid-scale mixing at the inversion, which also contributes to the higher entrainment rate seen with these models. We have drawn upon the theoretical and experimental results of Fernando and Hunt (1997) and McGrath et al. (1997) to argue that, because of the large buoyancy jump at the inversion, entrainment in the DYCOMS-II case is expected to be due primarily to breaking internal waves and hence that gradient-diffusion SGS models should indeed switch off subgrid-scale fluxes at the inversion.

This does not, however, prove that DSM is doing the right thing for the right reason. The DYCOMS-II results were compared with the results of Kirkpatrick and Armfield (2005), who tested DSM for a case with lower Richardson number. This is a more critical test case for DSM, since entrainment here is due to a different mechanism in which SGS mixing is expected to make a significant contribution to the entrainment. Thus, the subgrid model should predict significant SGS fluxes across the interface. DSM, however, exhibited similar behavior to that seen in the DYCOMS-II case, and consequently gave an underprediction of the entrainment rate.

Kirkpatrick and Armfield (2005) suggested that the tendency for DSM to calculate minimal SGS fluxes at an interface is due, at least in part, to the plane averaging used to stabilize the model. The authors noted that this averaging procedure is not valid on a plane that intersects a deforming interface as the plane will contain zones of both nonturbulent and turbulent flow. A more serious problem, however, may be that DSM switches off SGS fluxes as a result of insufficient reso-

lution of the energetic scales of turbulence in these regions. This also has implications for nondynamic SGS models, since their derivations are typically based on the same assumptions as those underlying the dynamic procedure.

The original concept of large-eddy simulation was that if one can provide sufficient resolution to ensure that the cutoff wavenumber lies in the inertial subrange, only the dissipative scales of turbulence need to be parameterized. Consequently only a relatively simple subgrid-scale turbulence model would be required. This theory has been shown to be valid through countless investigations, with good results obtained using the simplest models such as the classical Smagorinsky model, as long as there is adequate resolution. The fundamental problem, however, is that in the vast majority of cases of practical importance, whether they be engineering or environmental flows, there are regions of the domain where it is not possible to provide enough resolution to ensure that the energetic scales of turbulence are adequately resolved. In other words the original assumption of LES in these regions is not valid.

Despite this, the vast majority of work in the LES field has focused on developing more and more complex models that continue to assume a cutoff wavenumber in the inertial subrange. Consequently, while these new models show some improvements in predicting higher-order statistics in well-resolved turbulence they continue to fail dismally in regions such as the near-surface region and the entrainment layer. Here they either require ad hoc modifications or need to be combined with extra models in order to achieve acceptable results for even first-order statistics.

We believe future research should recognize that, contrary to the original LES concept, SGS models developed for practical applications need to have inherent in their design the capability to parameterize all scales of turbulence. They must adapt from parameterizing just the dissipative scales in well-resolved regions of the flow, up to parameterizing the full turbulence spectrum in poorly resolved regions. Clearly this requires a completely fresh approach to model development. We suggest that the critical feature of this "new generation" of SGS models be that they are based on the assumption that the cutoff wavenumber might lie *anywhere* in the turbulence spectrum.

Acknowledgments. We thank J. H. Ferziger, R. L. Street, F. K. Chow, R. T. Cederwall, and I. Senocak for helpful discussions regarding the subgrid-scale and near-surface models. We also thank B. Stevens for providing the DYCOMS-II measurements to the Eighth GCSS Boundary Layer Cloud Workshop and for his insightful suggestions on ways to improve our original manuscript.

REFERENCES

Ackerman, A. S., M. P. Kirkpatrick, D. E. Stevens, and O. B. Toon, 2004: The impact of humidity above stratiform clouds on indirect aerosol climate forcing. *Nature,* **432,** 1014–1017.

Boivin, M., O. Simonin, and K. D. Squires, 2000: On the prediction of gas-solid flows with two-way coupling using large eddy simulation. *Phys. Fluids,* **12,** 2080–2090.

Branley, N., and W. P. Jones, 2001: Large eddy simulation of a turbulent non-premixed flame. *Combust. Flame,* **127,** 1914–1934.

Bretherton, C. S., and M. C. Wyant, 1997: Moisture transport, lower tropospheric stability, and decoupling of cloud-topped boundary layers. *J. Atmos. Sci.,* **54,** 148–167.

——, and Coauthors, 1999: An intercomparison of radiatively driven entrainment and turbulence in a smoke cloud; as simulated by different numerical models. *Quart. J. Roy. Meteor. Soc.,* **125** (Part B), 391–423.

Brown, A. R., J. M. Hobson, and N. Wood, 2001: Large-eddy simulation of neutral turbulent flow over rough sinusoidal ridges. *Bound.-Layer Meteor.,* **98,** 411–441.

Carati, D., G. S. Winckelmans, and H. Jeanmart, 2001: On the modelling of the subgrid-scale and filtered-scale stress tensors in large-eddy simulation. *J. Fluid Mech.,* **441,** 119–138.

Cederwall, R. T., 2002: Large-eddy simulation of the evolving stable boundary layer over flat terrain. Ph.D. thesis, Stanford University, 231 pp.

Chow, F. K., R. L. Street, M. Xue, and J. H. Ferziger, 2005: Explicit filtering and reconstruction turbulence modeling for large-eddy simulation of neutral boundary layer flow. *J. Atmos. Sci.,* **62,** 2058–2077.

Clark, T. L., 1979: Numerical simulations with a three-dimensional cloud model: Lateral boundary condition experiments and multicellular severe storm simulations. *J. Atmos. Sci.,* **36,** 2191–2215.

Deardorff, J. W., 1980: Stratocumulus-capped mixed layers derived from a three-dimensional model. *Bound.-Layer Meteor.,* **18,** 495–527.

Esau, I., 2004: Simulation of Ekman boundary layers by large eddy simulation model with dynamic mixed subfilter closure. *Environ. Fluid Mech.,* **4,** 273–303.

Fernando, H. J. S., and J. C. R. Hunt, 1997: Turbulence, waves and mixing at shear-free density interfaces. Part 1. A theoretical model. *J. Fluid Mech.,* **347,** 197–234.

Germano, M., U. Piomelli, P. Moin, and W. H. Cabot, 1991: A dynamic subgrid-scale eddy viscosity model. *Phys. Fluids A,* **3,** 1760–1765.

Ghosal, S., and P. Moin, 1995: The basic equations for the large eddy simulation of turbulent flows in complex geometry. *J. Comput. Phys.,* **118,** 24–37.

Kirkpatrick, M. P., and S. W. Armfield, 2005: Experimental and large eddy simulation results for the purging of salt water from a cavity by an overflow of fresh water. *Int. J. Heat Mass Transfer,* **48,** 341–359.

——, N. N. Mansour, A. S. Ackerman, and D. E. Stevens, 2003: Dynamic turbulence modelling in large-eddy simulations of the cloud-topped atmospheric boundary layer. CTR Annual Research Briefs, Center for Turbulence Research.

Kosović, B., 1997: Subgrid-scale modelling for the large-eddy

simulation of high-Reynolds-number boundary layers. *J. Fluid Mech.,* **336,** 151–182.

Lappen, C. L., and D. A. Randall, 2001: Toward a unified parameterization of the boundary layer and moist convection. Part III: Simulations of clear and cloudy convection. *J. Atmos. Sci.,* **58,** 2052–2072.

Lilly, D. K., 1962: On the numerical simulation of buoyant convection. *Tellus,* **14,** 148–172.

——, 1992: A proposed modification of the Germano subgrid scale closure method. *Phys. Fluids A,* **4,** 633–635.

Linden, P. F., 1973: The interaction of vortex rings with a sharp density interface: A model for turbulent entrainment. *J. Fluid Mech.,* **60,** 467–480.

MacVean, M. K., and P. J. Mason, 1990: Cloud top entrainment instability through small-scale mixing and its parameterization in numerical models. *J. Atmos. Sci.,* **47,** 1012–1030.

Mason, P. J., 1985: A numerical study of cloud streets in the planetary boundary-layer. *Bound.-Layer Meteor.,* **32,** 281–304.

——, 1989: Large-eddy simulation of the convective atmospheric boundary-layer. *J. Atmos. Sci.,* **46,** 1492–1516.

——, 1994: Large-eddy simulation: A critical review of the technique. *Quart. J. Roy. Meteor. Soc.,* **120** (Part A), 1–26.

——, and D. J. Thomson, 1992: Stochastic backscatter in large-eddy simulations of boundary-layers. *J. Fluid Mech.,* **242,** 51–78.

McGrath, J. L., H. J. S. Fernando, and J. C. R. Hunt, 1997: Turbulence, waves and mixing at shear-free density interfaces. 2. Laboratory experiments. *J. Fluid Mech.,* **347,** 235–261.

Moeng, C. H., 1984: A large-eddy-simulation model for the study of planetary boundary-layer turbulence. *J. Atmos. Sci.,* **41,** 2052–2062.

Ogura, Y., and N. Phillips, 1962: Scale analysis of deep and shallow convection in the atmosphere. *J. Atmos. Sci.,* **19,** 173–179.

Piomelli, U., and J. Liu, 1995: Large eddy simulation of rotating channel flows using a localized dynamic model. *Phys. Fluids,* **7,** 839–848.

Porté-Agel, F., C. Meneveau, and M. B. Parlange, 2000: A scale-dependent dynamic model for large-eddy simulation: Application to a neutral atmospheric boundary layer. *J. Fluid Mech.,* **415,** 261–284.

Schumann, U., 1975: Subgrid scale model for finite difference simulation of turbulent flows in plane channels and annuli. *J. Comput. Phys.,* **18,** 376–404.

Scotti, A., C. Meneveau, and M. Fatica, 1997: Dynamic Smagorinsky model on anisotropic grids. *Phys. Fluids,* **9,** 1856–1858.

Smagorinsky, J., 1963: General circulation experiments with the primitive equations. I. The basic experiment. *Mon. Wea. Rev.,* **91,** 99–164.

Stevens, B., 2000: Cloud-transitions and decoupling in shear-free stratocumulus topped boundary layers. *Geophys. Res. Lett.,* **27,** 2557–2560.

——, and Coauthors, 2001: Simulations of trade wind cumuli under a strong inversion. *J. Atmos. Sci.,* **58,** 1870–1891.

——, and ——, 2003a: Dynamics and chemistry of marine stratocumulus—DYCOMS-II. *Bull. Amer. Meteor. Soc.,* **84,** 579–593.

——, and ——, 2003b: On entrainment rates in nocturnal marine stratocumulus. *Quart. J. Roy. Meteor. Soc.,* **129,** 3469–3492.

——, and ——, 2005: Evaluation of large-eddy simulations via observations of nocturnal marine stratocumulus. *Mon. Wea. Rev.,* **133,** 1443–1462.

Stevens, D. E., and C. S. Bretherton, 1996: A forward-in-time advection scheme and adaptive multilevel flow solver for nearly incompressible atmospheric flow. *J. Comput. Phys.,* **129,** 284–295.

——, J. B. Bell, A. S. Almgren, V. E. Beckner, and C. A. Rendleman, 2000: Small-scale processes and entrainment in a stratocumulus marine boundary layer. *J. Atmos. Sci.,* **57,** 567–581.

——, A. S. Ackerman, and C. S. Bretherton, 2002: Effects of domain size and numerical resolution on the simulation of shallow cumulus convection. *J. Atmos. Sci.,* **59,** 3285–3301.

Sullivan, P., and C. H. Moeng, 1992: An evaluation of the dynamic subgrid scale model in buoyancy driven flows. Preprints, *10th Symp. on Turbulence and Diffusion,* Portland, OR, Amer. Meteor. Soc., 82–87.

——, J. C. McWilliams, and C. H. Moeng, 1994: A subgrid-scale model for large-eddy-simulation of planetary boundary-layer flows. *Bound.-Layer Meteor.,* **71,** 247–276.

Wyant, M. C., C. S. Bretherton, H. A. Rand, and D. E. Stevens, 1997: Numerical simulations and a conceptual model of the stratocumulus to trade cumulus transition. *J. Atmos. Sci.,* **54,** 168–192.

Zang, Y., R. Street, and J. R. Koseff, 1993: A dynamic mixed subgrid-scale model and its application to recirculating flows. *Phys. Fluids A,* **5,** 3186–3196.